A Facile Peroxo-Precursor Synthesis Method and Structure Evolution of Large Specific Surface Area Mesoporous BaSnO₃

Chuande Huang,[†,‡] Xiaodong Wang,*[,†] Quan Shi,*[,†] Xin Liu,[†] Yan Zhang,[§] Fei Huang,[†,‡] and Tao Zhang[†]

[†]Dalian Institute of Chemical Physics, Chinese Academy of Sciences, Dalian 116023, China
[‡]University of Chinese Academy of Sciences, Beijing 100049, China
[§]Qingdao Institute of Bioenergy and Bioprocess Technology, Chinese Academy of Sciences, Qingdao 266101, China

Ⓢ Supporting Information

ABSTRACT: In this paper, we propose a facile and efficient strategy for synthesizing mesoporous BaSnO₃ with a surface area as large as 67 m²/g using a peroxo-precursor decomposition procedure. As far as we know, this is the largest surface area reported in literature for BaSnO₃ materials and may have a potential to greatly promote the technological applications of this kind of functional material in the area of chemical sensors, NOₓ storage, and dye-sensitized solar cells. The structure evolution of the mesoporous BaSnO₃ from the precursor was followed using a series of techniques. Infrared analysis indicates large amount of protons and peroxo ligands are contained in the peroxo-precursor. Although the crystal structure of the precursor appears cubic according to the analysis of X-ray diffraction data, Raman and Mössbauer spectroscopy results show that the Sn atom is offset from the center of [SnO₆] octahedron. After calcination at different temperatures, the precursor gradually transforms into BaSnO₃ by release of water and oxygen, and the distortion degree of [SnO₆] octahedral decreases. However, a number of oxygen vacancies are generated in the calcined samples, which are further confirmed by the physical property measurement system, and they would lower the local symmetry to some content. The concentration of the oxygen vacancies reduces simultaneously as the calcination temperature increases, and their contributions to the total heat capacity of the sample are calculated based on theoretical analysis of heat capacity data in the temperature region below 10 K.
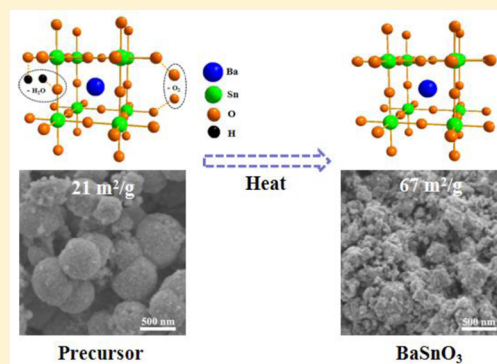
1. INTRODUCTION

BaSnO₃ is an n-type semiconductor with a band gap of 3.1 eV that has been widely studied by many researches due to its outstanding electric, photovoltaic, and optical nature.[1−3] It has been found that BaSnO₃ behaves with an ultrahigh sensitivity to a series of gases, such as CO, O₂, H₂, CH₄, H₂O, and ethanol, which may be applicable in the devleopment of innovative chemical gas and humidity sensors based on this kind of material.[4−8] Besides, BaSnO₃ is a potential material for reducing NOₓ emission of diesel or lean-burn engines because of its fantastic NOₓ sorption−desorption property.[9,10] Studies by Kim et al.[11] and Shin et al.[12] showed that BaSnO₃ exhibited fantastic performance when used as photoanode materials for dye-sensitized solar cells (DSSCs). La-doped BaSnO₃ was reported to be a promising candidate for transparent conducting oxides (TCOs), and its electrical mobility could reach as large as 320 cm² V⁻¹ s⁻¹, which is the largest value of all TCOs reported in literature.[13−16]

BaSnO₃ crystals belongs to an ideal cubic perovskite structure (space group $Pm3m$), in which Ba²⁺ ions locate at the center of the cell, while Sn⁴⁺ ions occupy the corner of the cube, and each Sn atom sixfold coordinated to oxygen sits at the center of the perfect octahedron.[17] This local crystal structure is closely related to the physical properties of BaSnO₃ stated above, and many researchers attempted to understand this particular feature in their work. For example, Liu et al.[15] studied the origin of the superior conductivity of BaSnO₃ in depth using the first-principle band structure calculations, and pointed out that the local structure distortion and strength of Sn−O hybridization were two important factors that were likely to affect the materials' conductivity. Hadjarab et al.[18] suggested that the oxygen deficiency in the BaSnO₃ structure could play a crucial role in achieving a high conductivity in the material.

Another technically important aspect involved in this research field is the surface area investigations of BaSnO₃-based materials since it may be applicable for fabricating high-performance chemical gas or humidity sensors, NOₓ storage medium, and DSSCs. Li et al.[19] found that SnO₂ with higher surface area was more sensitive to H₂ gas. Studies by Xu et al.[20] showed that the sensitivity of SnO₂ to CO was significantly enhanced by increasing the surface-to-volume ratio of SnO₂.

Tao et al.[21] pointed out that gas-sensing property of $BaSnO_3$ was surface-reaction controlled. In addition, preparation of crystalline $BaSnO_3$ with high surface area is important to improve the dye loading on DSSC photoanodes.[11] Guo et al.[22] showed that the performance of cell with dye-sensitized $BaSnO_3$ electrodes was dramatically elevated by increasing the dye loading from 1.08×10^{-7} to 2.17×10^{-7} mol·cm^{-2}. It turns out that the key step of making the $BaSnO_3$ materials applicable in these areas is to explore a way of obtaining larger specific surface areas in the material, and a number of researchers have proposed various $BaSnO_3$ synthesis techniques for this purpose.

The conventional $BaSnO_3$ synthesis procedure is to sinter the corresponding mixed starting materials at temperatures of ca. 1200 °C through a solid-state reaction. However, this method normally leads to polycrystalline $BaSnO_3$ with serious agglomerations and consequently low surface areas.[23,24] To lower the crystallization temperature and suppress grain growth, many approaches have been reported, including hydrothermal synthesis, microemulsion method, alkoxide hydrolysis synthesis, sol–gel method, peroxide route, and so on.[25−31] Most of these methods are focusing on improving the surface area of $BaSnO_3$ by decreasing the particle size in the preparation. However, it does not seem to be efficient. For example, $BaSnO_3$ (ca. 40 nm) prepared by sol–gel method and calcined at 750 °C for 4 h showed a surface area of only 14 m^2/g.[10] The surface area of $BaSnO_3$ (30−60 nm) obtained by hydrothermal preparation at 260 °C was only 5.3 m^2/g.[30] A surface area of ca. 25 m^2/g was achieved for $BaSnO_3$ (30 nm) synthesized via a wet chemical peroxide route and calcined at 800 °C, but its preparation condition was rigorous (10 °C under argon protection), and the pure $BaSnO_3$ appeared at a relatively high temperature of 900 °C.[31] Besides decreasing the particle size, fabrication of porous structures is also proposed to be effective in increasing the surface area.[32,33] Li et al.[34] prepared one-dimensional porous $BaSnO_3$ hollow architectures by releasing CO_2 from solid-state reaction between $BaCO_3$ core and SnO_2 shell, and a surface area of ca. 13 m^2/g was obtained. Buscaglia et al.[35] have synthesized porous $BaSnO_3$ with a specific surface area of 30−40 m^2/g by heating the $BaSn(OH)_6$ precursor (ca. 2 m^2/g) at 400 °C. It is worth noting that most of these works are related to high surface area achievement, but few focus on understanding the structure evolution of $BaSnO_3$ during the synthesis procedure. Köferstein et al.[36] reported that an unknown barium tin oxycarbonate intermediate phase $(BaSnO(CO_3)_2)$ was formed in the phase evolution of the $[Ba(C_2H_6O_2)_4][Sn(C_2H_4O_2)_3]$ precursor to $BaSnO_3$.

In this work, we present a facile method of synthesizing mesoporous $BaSnO_3$ with large specific surface areas by the decomposition of a peroxo-precursor, which is prepared through reacting barium carbonate with stannate in basic hydrogen peroxide solution. The as-prepared $BaSnO_3$ obtained by calcination of the peroxo-precursor at 500 °C shows a specific surface area as large as 60−70 m^2/g, which is the largest value reported in literature for $BaSnO_3$ as far as we know. The structure evolution from the precursor to final $BaSnO_3$ products is systematically investigated using X-ray diffraction (XRD), scanning electron microscopy (SEM), thermogravimetry (TG), differential thermal analysis (DTA), mass-spectra (MS) with temperature-programmed desorption (TPD), infrared (IR) analysis, Raman spectroscopy, and ^{119}Sn Mössbauer spectroscopy. In addition, the $BaSnO_3$ samples prepared from sintering the precursor above 400 °C were measured using a

physical property measurement (PPMS) system in the temperature range from 1.9 to 300 K, and the results indicate a significant linear heat capacity contribution of the oxygen vacancies existing in the materials. The enthalpies of these samples at 298.15 K are also calculated based on the curve fitting of the experimental heat capacity data.

2. EXPERIMENTAL SECTION

2.1. Material Preparation. All reagents in the preparation procedure were of analytical reagent grade and used without further purification. The starting solution was prepared by dissolving $SnCl_4 \cdot 5H_2O$ (2 mmol; 99%, Kermel, Tianjin, China) in a transparent H_2O_2 aqueous solution (40 mL; 30%, Kermel, Tianjin, China) with a pH value ∼9, which was adjusted by dropwise addition of ammonia solution (25%, Kermel, Tianjin, China) into the solution with magnetic stirring. Subsequently, $BaCO_3$ powders (2 mmol; S_{BET} = 1.8 m^2/g; 99%, Kermel, Tianjin, China) were introduced to the solution at room temperature, forming a suspension that was then heated to 95 °C and kept for 5 h in a water bath. A white precipitate was generated during this process. The precipitate was filtered from the solution and then washed with deionized water until the pH of filtrate was ∼7, and a peroxo-precursor was then obtained by drying the precipitate overnight in an oven at 120 °C (marked as BS-120). The peroxo-precursor was calcined in static air at 200, 300, 400, 500, 600, and 800 °C for 4 h, respectively, and finally the $BaSnO_3$ products were obtained and denoted as BS-T (T represents the calcination temperature). For comparison, SnO_2 precursor was prepared in the absence of $BaCO_3$ undergoing the same procedure (precipitated at 95 °C, filtered, washed and dried at 120 °C), and marked as S-120.

2.2. Characterization. The phase composition was examined at room temperature using a PANalytical X'Pert-Pro powder X-ray diffractometer with Cu Kα radiation (λ = 0.1541 nm). IR analysis was performed over the range of 400−4000 cm^{-1} on a Fourier transform infrared (FT-IR) spectrometer (Bruker Equinox 55) in the form of KBr discs. TG and DTA were performed on TA Q600 equipment in dry air atmosphere with a constant heating rate of 10 °C/min. An independent MS (OMNISRAR) analysis with He as carrier gas was used to monitor the gases released during the TPD experiment (constant heating rate of 10 °C/min). N_2 adsorption−desorption analysis was performed on a Quadrasorb SI instrument. Before the measurements, the BS-120, BS-200, and BS-300 samples were degassed in vacuum for 5 h at 100, 150, and 250 °C, respectively. The other samples (BS-400, BS-500, BS-600, and BS-800) were degassed at 300 °C in vacuum for 5 h. The specific surface area was calculated using a Brunauer−Emmett−Teller (BET) method over the range of P/P_0 from 0.05 to 0.30.[37,38] The Barrett−Joyner−Halenda (BJH) pore size distribution curves were obtained according to the adsorption branches of the isotherms. The morphologies of all samples were investigated using field-emission SEM (JEOL JSM-7800F). The Raman spectroscopy was recorded using a Jobin LabRAM HR 800 spectrophotometer equipped with an Ar laser (532 nm). The room-temperature Mössbauer spectra were recorded using ^{119}Sn as the radiation source ($BaSnO_3$ matrix), and the isomer shifts were shown with respect to $BaSnO_3$ at room temperature.

The crystallite sizes of the calcined samples were calculated using Scherer formula without the consideration of strain:[39] $D = 0.9\lambda/B \cos\theta$, where θ is the diffraction angle, B indicates the full width at half-maximum, and λ is the wavelength of the incident X-rays (0.1541 nm).

The heat capacities of BS-400, BS-500, BS-600, and BS-800 samples were measured using a Quantum Design PPMS in zero magnetic field with logarithmic spacing from 1.9 to 100 K and in 10 K intervals from 100 to 300 K. The heat capacity measurement accuracy was verified by measuring a high-purity copper pellet and found to be ±2% below 20 K and within ±1% from 20 to 400 K. The powdered sample was measured using a technique developed by Shi et al.,[40,41] which can achieve an accuracy of ±2% below 10 K and ±1% from 10 to 300 K. The detailed sample preparation and calorimetric procedure can be found in refs 36 and 37. The sample mass used in the measurement is
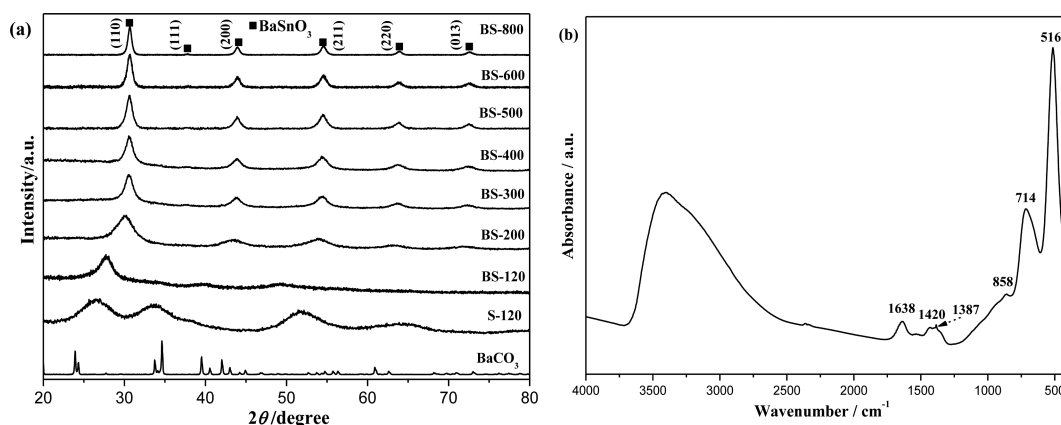
Figure 1. (a) XRD patterns of $BaCO_3$ starting powder, S-120, and BS-T, and (b) FT-IR spectrum of BS-120.
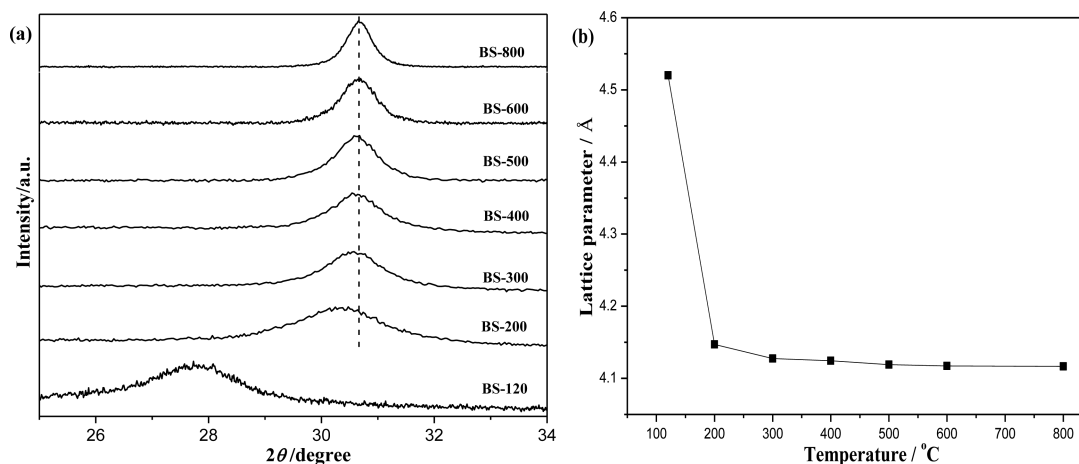

Figure 2. (a) Magnified XRD patterns of BS-T at $25° \leq 2\theta \leq 34°$, and (b) lattice parameter calculated for BS-T samples.

18.03, 22.07, 24.90, and 23.32 mg for BS-400, BS-500, BS-600, and BS-800, respectively.

3. RESULTS AND DISCUSSION

XRD patterns of the precursor of BS-120, the SnO_2 precursor of S-120, and the $BaCO_3$ starting material are shown in Figure 1a. It can be seen that BS-120 exhibits a uniform phase without any observable traces of $BaCO_3$ and SnO_2. The structure details of BS-120 are further investigated by FT-IR spectra in Figure 1b. It can be seen that a broad band appearing from 2500 to 3700 cm^{-1} could be attributed to O−H stretching mode from water and SnO−H groups, while the peak located at 1638 cm^{-1} may be ascribed to the contribution of δ(H−O−H) vibration.[42,43] A broad envelope at 1420 cm^{-1} and a shoulder at 858 cm^{-1}, which are assigned to δ(O−O−H) and ν(O−O) vibrations, respectively, could be observed, indicating the presence of peroxo ligands in the precursor.[43] The peaks at 516 and 714 cm^{-1} can be ascribed to vibrations of Sn−OH and Sn−O−Sn in the precursor, respectively.[29,42] Besides, a weak and sharp band existing at 1387 cm^{-1} in the spectra resulting from ν(C−O) vibrations can be observed from the FT-IR spectra, suggesting that some carbonate impurities might be included in BS-120.[43] However, these impurity contents are relatively small, could not be detected in the XRD patterns, and therefore can be ignored in the following $BaSnO_3$ synthesis from the peroxo-precursor.

The XRD pattern evolution of the $BaSnO_3$ obtained by calcination of the peroxo-precursor at different temperatures is also included in Figure 1a. As can be seen from the figure, all BS-T samples reveal a single phase with cubic perovskite lattice. Besides, the prominent reflection peak of BS-120 around 27.8° shifts to the higher 2θ positions in the $BaSnO_3$ samples, which is illustrated more clearly by the magnified view ($25° \leq 2\theta \leq 34°$) in Figure 2a. Such a shift is likely due to the lattice parameters decreasing gradually during the $BaSnO_3$ formation process with the calcination temperature increasing. For BS-T samples calcined at above 400 °C, all of the diffraction peaks could be well-indexed to the standard patterns of the cubic $BaSnO_3$ phase [JCPDS 89−2488], suggesting that these samples have transferred to a $BaSnO_3$ phase. Also, the crystallite sizes were estimated to be 8.9, 10.7, 12.7, and 17.9 nm for BS-400, BS-500, BS-600, and BS-800, respectively, based on the full width half maxima of the prominent (110) reflection in the XRD patterns using the Scherer's equation. To further detect the lattice evolution during the calcination process, the lattice constant a of all BS-T samples were calculated, and the results are presented in Figure 2b. Note that the most significant decline of lattice parameter is observed between BS-120 and BS-200 (from 4.520 to 4.147 Å), and then the value of the unit cell edge decreases slowly with the increase of calcination temperatures. After calcined above 500 °C, the lattice constant a of BS-T samples can be maintained at ~4.119 Å, which coincides with the reported value of 4.118 Å in literature for $BaSnO_3$.[44]

To probe the structure evolution of BS-T samples during the calcination process, the decomposition feature of BT-120 was

monitored using the TG-DTA and MS techniques. The total weight loss values of BS-T samples from the TG analysis are summarized in Table 1. Combining both measurement results,

Table 1. Total Weight Loss, Surface Area, Pore Volume and C Constant of BS-T Samples

samples	weight loss (%)	surface area (m^2/g)	pore volume (cm^3/g)	C constant
BS-120	12.3	21.2	0.055	107
BS-200	8.5	20.1	0.076	96
BS-300	5.4	14.0	0.069	146
BS-400	2.9	40.1	0.081	80
BS-500	1.9	67.2	0.087	56
BS-600	1.1	36.9	0.079	84
BS-800	0.1	28.0	0.081	99

as shown in Figure 3, the decomposition process of BS-120 precursor can be divided into three distinct steps as the temperature increases from room temperature to 800 °C. The first step is below 150 °C where a small weight loss (∼1%) appears in TG-DSC and only water content is observed in MS, indicating that a small amount of weakly bonded water or hydroxyl groups are evaporated from BT-120. The second step can be identified in the temperature range from 150 to 400 °C. In this step, a significant amount of weight loss of ca. 9% and relatively large water and oxygen signals are found in TG-DSC and MS curves, respectively, suggesting that a large number of water and oxygen are rapidly released in this temperature region. Additionally, two exothermal peaks can be noticed in the heat flow curve as shown in Figure 3a, which is likely due to the decomposition process of peroxo groups into oxygen. However, it is clearly shown that this process could be finished mainly below 400 °C since no more oxygen signal can be found at higher temperatures in the MS curve.

As for the last step above 400 °C, only a small amount of water loss (2%) can be detected, which is likely attributed to the strongly bonded hydroxyl groups released from the precursor at high temperatures. It is suggested that, compared to the peroxo groups, the strongly bonded hydroxyl groups are relatively difficult to be removed from the precursor during the calcinations process. In addition, a trace of CO_2, which could result from the decomposition of the carbonate impurities from the precursor, can be noticed in the MS curve in this step. On the basis of the fact of this BS-120 decomposition process, it is reasonable to conclude that the large lattice constant of BS-120

mentioned in the above XRD results is likely due to a multitude of hydroxyl and peroxo ligands incorporated in the sample, and the significant decline of lattice constant of BT-120 to those of $BaSnO_3$ samples may be on account of a significant amount of hydroxyl and peroxo ligands removed from the precursor in the second step.

The BET surface areas of all BS-T samples obtained using the N_2 adsorption at the temperature of −196 °C are listed in Table 1. It can be seen that the surface area slowly decreases from BT-120 to BT-300, increases greatly from BT-300 to BT-500, reaches the largest value of 67.2 m^2/g, and then decreases again from BT-500 to BT-800. Such a surface area evolution could be understood from a competition between the particle growth and the mesoporous structure formation due to the water and oxygen removal during the calcination process. At low temperatures, only the small amount of weakly bonded water or hydroxyl groups are removed, with most of the hydroxyl and peroxo ligands remaining in the sample, and consequently the surface area does not change significantly. However, as the temperature continues increasing to 500 °C, a large number of water and oxygen is released, and a mesoporous structure formation could be expected in the samples, which can be confirmed in the following nitrogen adsorption−desorption isotherm and SEM determination. Although the particle size would grow with increasing calcination temperature, the mesoporous structure formation is predominant during this process. As the sample calcined at higher temperatures, the particles prefer to aggregate together with the mesoporous structure gradually disappearing, and therefore the surface area tends to decrease. It is worth mentioning that the surface area of 67.2 m^2/g achieved in BT-500 is the largest value reported in literature, as far as we know, and also can be maintained a relatively large value of ∼30 m^2/g even at the higher calcination temperature of 800 °C. It suggests that the peroxo-precursor decomposition method is a efficient way to synthesize $BaSnO_3$ materials with large surface areas.

To further explore the mesoporous structure of the $BaSnO_3$ samples, the nitrogen adsorption−desorption isotherms and the BJH pore size distribution curves of BS-T samples calcined from 400 to 800 °C are collected in Figure 4 (and Supporting Information, Figure S1). As can be seen in Figure 4a, all of these samples exhibit a type IV isotherm with a hysteresis loop, confirming that the mesoporous structure is formed in the samples. Taking the sample's decomposition process into account, the formation of the mesopores is mostly ascribed to
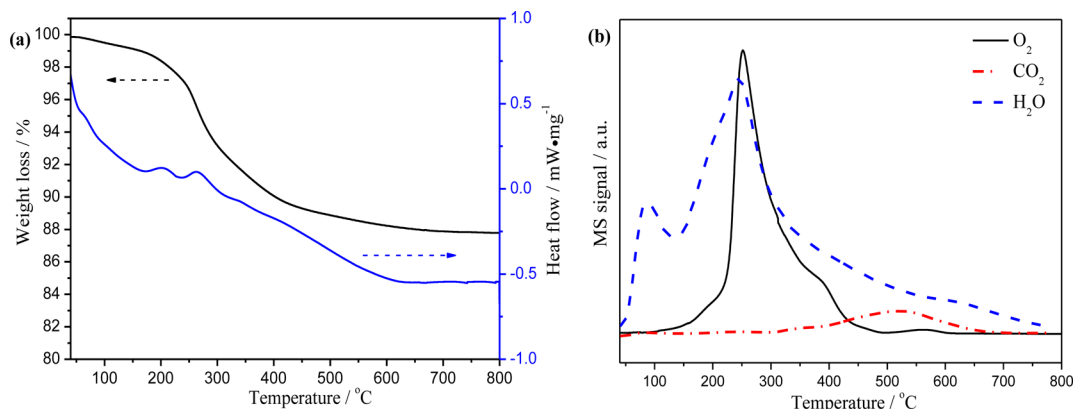

Figure 3. (a) TG-DTA curve for BS-120; (b) MS signals of the released gas during the heat-treatment of BS-120.
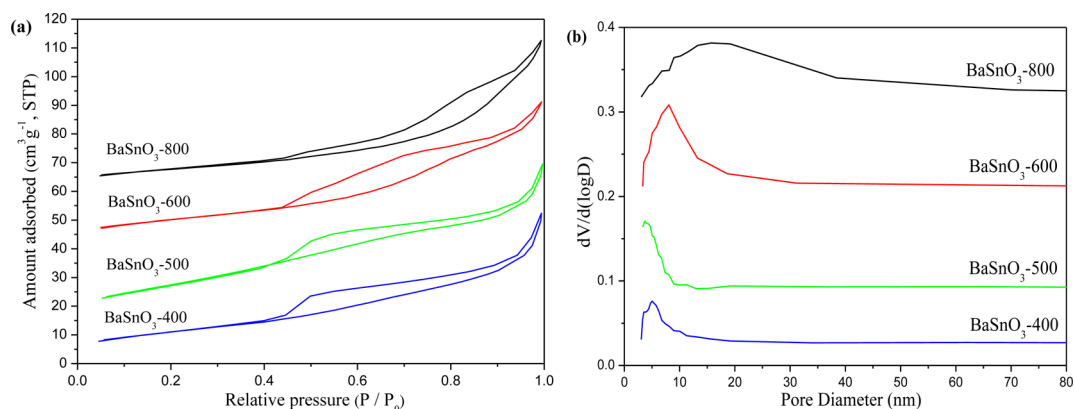
Figure 4. (a) N$_2$ physisorption isotherms and (b) pore size distribution plots (calculated from the adsorption branch) of BS-400, BS-500, BS-600, and BS-800. The N$_2$ sorption isotherms of BS-800, BS-600, and BS-500 are offset vertically by 60, 40, and 10 cm^3 g^{-1}, respectively.
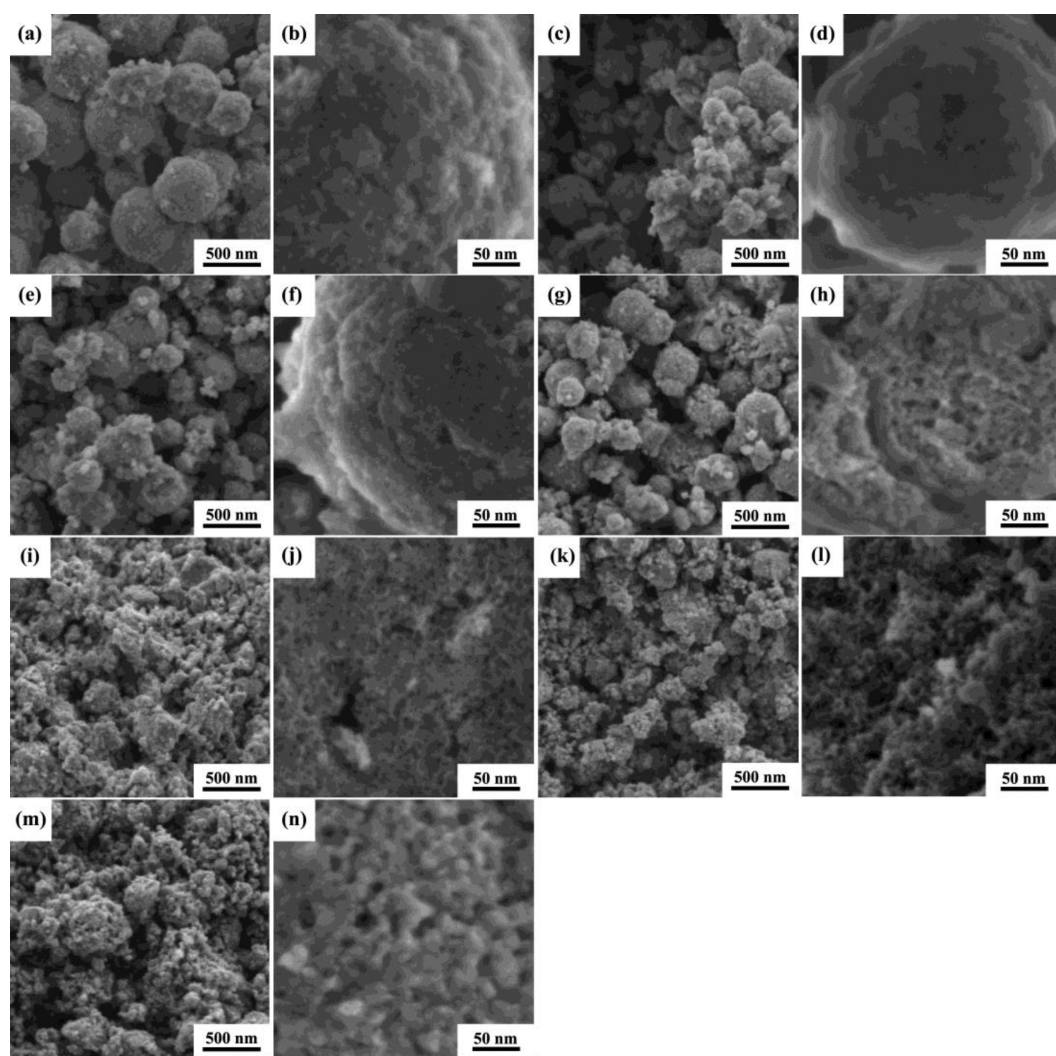

Figure 5. SEM images of (a, b) BS-120, (c, d) BS-200, (e, f) BS-300, (g, h) BS-400, (i, j) BS-500, (k, l) BS-600, and (m, n) BS-800.

release of water and oxygen from the precursor. The hysteresis loops vary from sample to sample indicating the differences in pore-size distribution (Figure 4b). For BS-400 and BS-500 samples, there is a sharp peak in the range from 3.5 to 8.0 nm, indicating that their pore size distributions are mainly concentrated in this region. However, in the case of BS-600 and BS-800, the pore size distribution is gradually widened as

the calcination temperature increases, revealing the BaSnO$_3$ particle growth during the calcination process.

The morphology of the BS-T samples calcined at different temperatures characterized by SEM is shown in Figure 5. Clearly, BS-120 (Figure 5a) mainly consists of spherical particles with sizes varying from 100 to a few hundred nanometers, and no noticeable pores can be detected on the

surface (Figure 5b). This spherical morphology does not change much until calcining the sample at 200 and 300 °C (Figure 5c–f). However, some mesopores could be observed on the surface of BS-400 (Figure 5h), which is likely to account for the surface area increasing at higher calcination temperatures. For the BT-500 sample (Figure 5i), the spherical structure of the precursor tends to collapse under the high internal pressure generated by the water and oxygen release, and consequently a number of nanoparticles with mesoporous structures can be obtained. As calcination temperatures increase to 600 and 800 °C (Figure 5k–n), the growth of BaSnO$_3$ particles is notable, and the pore size increases simultaneously. These observations are well-consistent with the N$_2$ adsorption–desorption results discussed above.

The structure evolution of the BS-120 precursor to the BS-T samples is investigated by ^{119}Sn Mössbauer spectra, from which the chemical state of Sn on a atomic scale can be detected with a high sensitivity based on the obtained values of isomer shift (IS) and quadrupole splitting (QS).[45] The IS value is closely related to the valence state and atomic spacing, while the QS value is sensitive to the symmetry of the charge around the Sn atom.[46] The experimental and fitted Mössbauer spectra data for BS-T and S-120 at room temperature are shown in Figure 6,
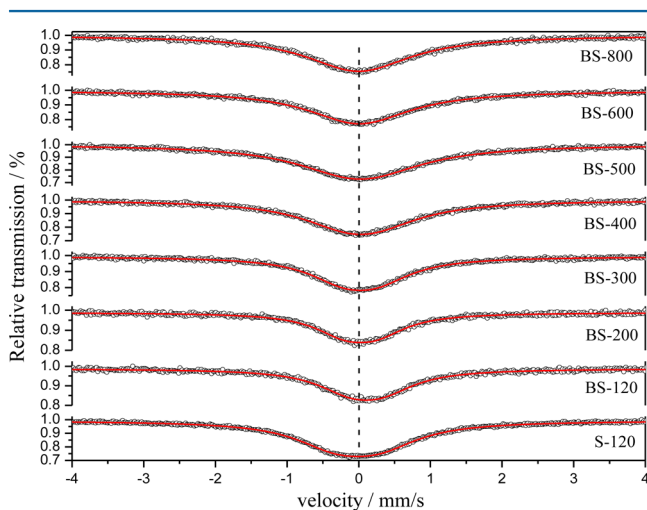

Figure 6. Room-temperature ^{119}Sn Mössbauer spectra of S-120 (bottom) and BS-T samples.

and the corresponding parameters are given in Table 2. The IS values of Sn^{4+} and Sn^{2+} are generally located in the range of (−0.4 to 2.0) mm/s and (2.3 to 4.5) mm/s (relative to

**Table 2. Room-Temperature ^{119}Sn Mössbauer Parameters**

samples	IS^a (mm/s)	QS^b (mm/s)	LW^c (mm/s)
S-120	−0.01	0.62	1.36
BS-120	0.07	0.51	1.40
BS-200	0.02	0.47	1.04
BS-300	0.02	0.44	1.22
BS-400	0.02	0.39	1.64
BS-500	0.02	0.30	1.99
BS-600	0.01	0.00	1.74
BS-800	0.00	0.00	1.78
Bulk BaSnO$_3$^{d}	0.00	0.00	

^{a}Isomer shift relative to BaSnO$_3$. ^{b}Quadrupole splitting. ^{c}Line width. ^{d}Data taken from ref 14.

BaSnO$_3$), respectively.[14] As for the IS values listed in Table 2, all of them are located in the (−0.4 to 2.0) mm/s region, indicating that the Sn atom in the BS-T and S-120 samples are exclusively in +4 oxidation state. Also, the IS values of BS-T samples tend to slightly decrease with increasing calcination temperature, revealing a decrease of the S electron density in the Sn atom. In other words, the Sn−O interaction in the BS-T samples presents as strengthened as the calcination process goes to higher temperatures.

As for the quadrupole splitting feature listed in Table 2, the QS values for BS-T (120 ≤ T ≤ 400) samples are much larger than that of bulk BaSnO$_3$ (0 mm/s),[14] suggesting that [SnO$_6$] octahedron is highly distorted because of the significant amount of the hydroxyl and peroxo groups included in the samples. And also, the slow reduction in the QS values with the temperature increase indicates that the symmetry of [SnO$_6$] octahedron is gradually improved with the water and oxygen removed from the sample.

According to the decomposition process discussed above, the hydroxyl groups and peroxo ligands are mostly removed after calcination at 500 °C. However, BS-500 still shows a low local symmetry since its QS value is found to be as high as 0.30 mm/s. This may be caused by oxygen vacancies that could be generated by the hydroxyl groups releasing during the calcination, and the corresponding reaction can be presented below:[47]

$$2OH^{\bullet}_O \rightarrow O^{\bullet\bullet}_O + V^{\bullet\bullet}_O + H_2O(g) \tag{1}$$
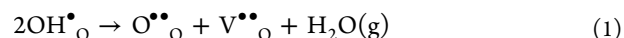
Further calcination at 600 and 800 °C leads to reduction of the QS values to ∼0 mm/s, giving a clue that most of [SnO$_6$] units are likely transformed into regular octahedrons and that the structure symmetry could be improved with the oxygen vacancies significantly removed from the sample.

The local structural distortions of BS-T samples were further investigated using the Raman spectroscopy, and the results are shown in Figure 7. According to group theory, single-crystal
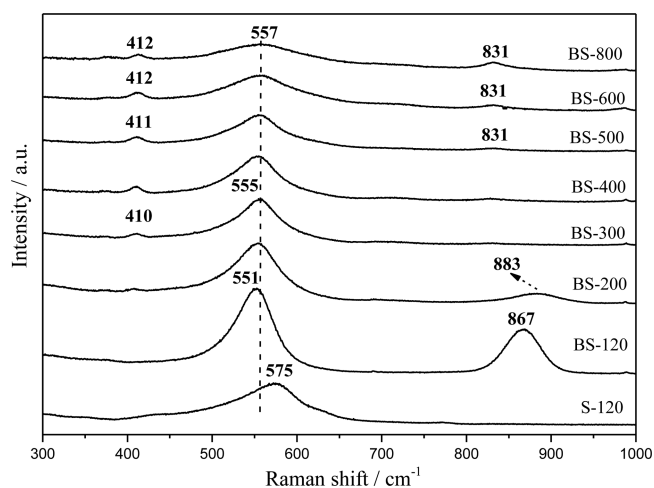

Figure 7. Raman spectrum of BS-T and S-120.

BaSnO$_3$ with a centrosymmetric structure belonging to *Pm3m* space group can exhibit nonfirst-order Raman active modes. Therefore, the activation of phonons for BS-T may account for an ideal cubic structure with a lower internal symmetry.[4,48] For BS-120, two Raman features can be observed at 551 and 867 cm^{-1}, which could be assigned to the Sn−O and Sn−O−O vibration modes, respectively.[49] The peak corresponding to

Sn−O−O vibration is significantly suppressed after calcination of the precursor at 200 °C because of the peroxo groups' decomposition. This result is in good agreement with the MS analysis (Figure 3b). The obvious blue shift of the peak for BS-200 may be ascribed to the increase of Sn−O−O interaction, and this deduction is confirmed by the TPD experiment where the desorption peak of oxygen (Supporting Information, Figure S2) is shifted to higher temperature of 286 °C. After calcination at 300 °C, the peak corresponding to the Sn−O−O vibration disappears, indicating that most of the peroxo groups have already vanished. Moreover, the stretching mode of Sn−O bond around 549 cm⁻¹ for BS-120 shifts to higher frequencies after calcination. This shift could be attributed to the strengthened Sn−O interaction based on the Mössbauer analysis. Most importantly, the shift between BS-120 and BS-200 is especially pronounced, which is consistent with the change of lattice parameters determined in the XRD patterns (Figure 2). It should be pointed out here that a similar Raman shift is also observed for BiVO₄ materials.[50,51] For BS-300 and BS-400, a new Raman band around 410 cm⁻¹ emerges, which is likely induced by oxygen vacancies according to the reports by Balamurugan et al.[52] and Guo et al.[48] Another characteristic band located at 831 cm⁻¹ is observed for BS-T samples calcined at 500, 600, and 800 °C, while the intensity of vibrational bands decrease significantly for BS-600 and BS-800. This may be explained by the fact that the structure symmetry is improved as the surface area reduces and the oxygen vacancies decrease.

The existence of oxygen vacancies is further confirmed by measuring low-temperature heat capacities of BS-400, BS-500, BS-600, and BS-800 using a PPMS, and the experimental results are shown in Figure 8. According to the MS results
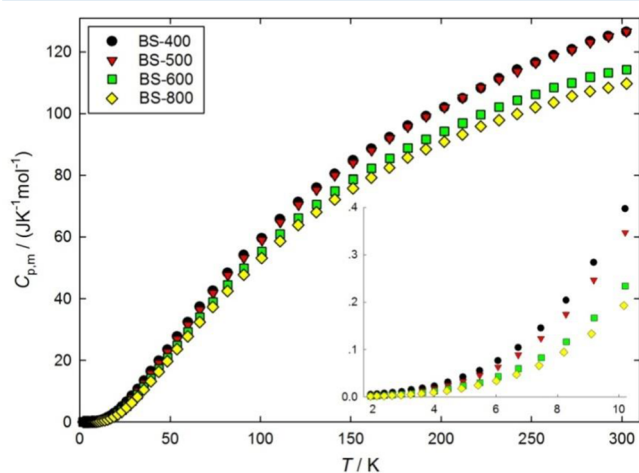

Figure 8. Plot of the experimental heat capacities of BS-T (*T* = 400, 500, 600, and 800) samples measured over the temperature range from 2 to 300 K. (inset) The data below 10 K.

(Figure 4b), the peroxo ligands have already been removed completely from these samples; therefore, the mass loss in the

TG experiment (Table 1) can be attributed to the water desorption. Consequently, the chemical formula of these BS-T samples used for molecular heat capacity calculation can be inscribed in the form of BaSnO₃·nH₂O, where the water content of *n* can be determined to be 0.504, 0.327, 0.187, and 0.017 for BS-400, BS-500, BS-600, and BS-800, respectively, based on the above TG measurements.[53,54]

The heat capacity of a substance at low temperature (normally below 25 K) can be treated as a sum of contributions from electrons, lattice vibrations, nuclei, magnons, and impurities.[55−57] Contributions of each property to the total heat capacity can be independently expressed using their corresponding theoretical functions. Therefore, some important information can be extracted by fitting the heat capacity data using these functions. For BS-T (*T* = 400, 500, 600, and 800) samples, the heat capacity data below 10 K was fitted using the following equation:

$$c_{p,m} = \gamma T + B_3 T^3 + B_5 T^5 + B_7 T^7 \tag{2}$$

where the γT is the contribution from the oxygen vacancies, and the rest represents the harmonic lattice model.[55,58,59] The fitted parameters are listed in Table 3. Note that the contribution of the oxygen vacancies to the total heat capacity decreases with increasing calcination temperature, revealing that the vacancies are gradually removed during the calcination process. This conclusion agrees well with the results obtained in the Mössbauer spectra and Raman spectroscopy analysis. Additionally, the thermodynamic functions of these BS-T samples were also calculated based on the curve fitting of the experimental heat capacities, and the standard molar entropies of BS-400, BS-500, BS-600, and BS-800 at 298.15 K have been determined to be 141.69, 139.78, 129.09, and 123.77 J·K⁻¹·mol⁻¹, respectively.

4. CONCLUSIONS

In the present work, we have developed a facile method for synthesizing large specific surface area mesoporous BaSnO₃ by preparing a peroxo-precursor and calcining the precursor at relatively low temperatures. The specific surface area of the BaSnO₃ obtained at the calcination temperature of 500 °C has been determined to be 67.2 m²/g, which is the largest surface area reported in literature as far as we know, and the sample can be maintained at the relatively high surface area of ca. 30 m²/g even at calcination temperatures up to 800 °C.

The structure evolution from the precursor to the BaSnO₃ samples during the calcination process has been extensively investigated using a variety of characterization techniques. The results have suggested that the precursor possesses a significant amount of hydroxyl and peroxo groups, which leads to a large unit cell edge of 4.520 Å, weak Sn−O interaction, and distorted [SnO₆] octahedral. After calcination at different temperatures, water and oxygen release during the calcination process and bring a mesoporous structure into the sample. Meanwhile, the lattice parameters decrease gradually, and Sn−O interactions

Table 3. Fitted Parameters for BS-T (*T* = 400, 500, 600, and 800) Samples

parameter	BS-400	BS-500	BS-600	BS-800
γ (J·K⁻¹·mol⁻¹)	2.05×10^{-3}	1.00×10^{-3}	4.69×10^{-4}	3.58×10^{-4}
B_3 (J·K⁻¹·mol⁻¹)	1.97×10^{-4}	1.76×10^{-4}	1.56×10^{-4}	1.21×10^{-4}
B_5 (J·K⁻¹·mol⁻¹)	2.83×10^{-6}	2.60×10^{-6}	6.40×10^{-7}	7.90×10^{-7}
B_7 (J·K⁻¹·mol⁻¹)	-1.29×10^{-8}	-1.23×10^{-8}	-4.40×10^{-10}	-2.05×10^{-9}

are strengthened. The symmetry of $[SnO_6]$ octahedron is also improved during this process. However, oxygen vacancies are generated simultaneously, which contributes to the distortion of $[SnO_6]$ octahedral as well.

The thermodynamic properties of $BaSnO_3$ samples calcined above 400 °C were studied by PPMS. The results indicate a significant linear heat capacity contribution of the oxygen vacancies existing in the materials, and the concentration of the vacancies tends to decrease with the calcination temperature increasing. The standard molar entropies (T = 298.15 K) of BS-400, BS-500, BS-600, and BS-800 are determined to be 141.69, 139.78, 129.09, and 123.77 $J\cdot K^{-1}\cdot mol^{-1}$, respectively, which are calculated based on the curve fitting of the experimental heat capacities.

■ ASSOCIATED CONTENT

Ⓢ Supporting Information

Illustrations featuring additional N_2 adsorption−desorption data and O_2 TPD profile. This material is available free of charge via the Internet at http://pubs.acs.org.

■ AUTHOR INFORMATION

Corresponding Authors

*E-mail: xdwang@dicp.ac.cn. Phone: +86 411 84379680. Fax: +86 411 84379680 (X. W.).
*E-mail: shiquan@dicp.ac.cn. Phone: +86 411 84379213 (Q. S.).

Notes

The authors declare no competing financial interest.

■ ACKNOWLEDGMENTS

■ REFERENCES

(1) Azad, A. M.; Hon, N. C. *J. Alloys Compd.* **1998**, *270*, 95−106.

(2) Mizoguchi, H.; Eng, H. W.; Woodward, P. M. *Inorg. Chem.* **2004**, *43*, 1667−1680.

(3) Mizoguchi, H.; Woodward, P. M.; Park, C. H.; Keszler, D. A. *J. Am. Chem. Soc.* **2004**, *126*, 9796−9800.

(4) Cerdà, J.; Arbiol, J.; Dezanneau, G.; Díaz, R.; Morante, J. R. *Sens. Actuators, B* **2002**, *84*, 21−25.

(5) Lampe, U.; Gerblinger, J.; Meixner, H. *Sens. Actuators, B* **1995**, *25*, 657−660.

(6) Cerda, J.; Morante, J. R.; Spetz, A. L. BaSnO₃ Oxygen Sensors without the Need of a Reference Electrode. *Proceedings of the IEEE Sensors 2003, Vols 1 and 2*; IEEE: New York, 2003; pp 1164−1165.

(7) Tao, S. W.; Gao, F.; Liu, X. Q.; Sorensen, O. T. *Sens. Actuators, B* **2000**, *71*, 223−227.

(8) Reddy, C. V. G.; Manorama, S. V.; Rao, V. J. *J. Mater. Sci.: Mater. Electron.* **2001**, *12*, 137−142.

(9) Hodjati, S.; Vaezzadeh, K.; Petit, C.; Pitchon, V.; Kiennemann, A. *Appl. Catal., B* **2000**, *26*, 5−16.

(10) Hodjati, S.; Vaezzadeh, K.; Petit, C.; Pitchon, V.; Kiennemann, A. *Catal. Today* **2000**, *59*, 323−334.

(11) Kim, D. W.; Shin, S. S.; Lee, S.; Cho, I. S.; Kim, D. H.; Lee, C. W.; Jung, H. S.; Hong, K. S. *ChemSusChem* **2013**, *6*, 449−454.

(12) Shin, S. S.; Kim, J. S.; Suk, J. H.; Lee, K. D.; Kim, D. W.; Park, J. H.; Cho, I. S.; Hong, K. S.; Kim, J. Y. *ACS Nano* **2013**, *7*, 1027−1035.

(13) Sallis, S.; Scanlon, D. O.; Chae, S. C.; Quackenbush, N. F.; Fischer, D. A.; Woicik, J. C.; Guo, J. H.; Cheong, S. W.; Piper, L. F. J. *Appl. Phys. Lett.* **2013**, *103*.

(14) Mizoguchi, H.; Chen, P.; Boolchand, P.; Ksenofontov, V.; Felser, C.; Barnes, P. W.; Woodward, P. M. *Chem. Mater.* **2013**, *25*, 3858−3866.

(15) Liu, H.-R.; Yang, J.-H.; Xiang, H. J.; Gong, X. G.; Wei, S.-H. *Appl. Phys. Lett.* **2013**, *102*.

(16) Kim, H. J.; Kim, U.; Kim, T. H.; Kim, J.; Kim, H. M.; Jeon, B.-G.; Lee, W.-J.; Mun, H. S.; Hong, K. T.; Yu, J.; Char, K.; Kim, K. H. *Phys. Rev. B: Condens. Matter* **2012**, *86*, 165205.

(17) Scanlon, D. O. *Phys. Rev. B: Condens. Matter* **2013**, *87*.

(18) Hadjarab, B.; Trari, M.; Kebir, M. *Mater. Sci. Semicond. Process.* **2015**, *29*, 283−287.

(19) Li, G. J.; Kawi, S. *Mater. Lett.* **1998**, *34*, 99−102.

(20) Xu, C.; Tamaki, J.; Miura, N.; Yamazoe, N. *Sens. Actuators, B* **1991**, *3*, 147−155.

(21) Tao, S.; Gao, F.; Liu, X.; Sørensen, O. T. *Sens. Actuators, B* **2000**, *71*, 223−227.

(22) Guo, F.-a.; Li, G.; Zhang, W. *Int. J. Photoenergy* **2010**, *2010*.

(23) Maekawa, T.; Kurosaki, K.; Yamanaka, S. *J. Alloys Compd.* **2006**, *416*, 214−217.

(24) Upadhyay, S.; Sahu, A. K.; Kumar, D.; Parkash, O. *J. Appl. Phys.* **1998**, *84*, 828−832.

(25) Lu, W.; Schmidt, H. *J. Eur. Ceram. Soc.* **2005**, *25*, 919−925.

(26) Lu, W.; Schmidt, H. *Ceram. Int.* **2008**, *34*, 645−649.

(27) Song, Y. J.; Kim, S. *J. Ind. Eng. Chem.* **2001**, *7*, 183−185.

(28) Stanulis, A.; Sakirzanovas, S.; Van Bael, M.; Kareiva, A. *J. Sol−Gel Sci. Technol.* **2012**, *64*, 643−652.

(29) Lu, W.; Schmidt, H. *J. Sol−Gel Sci. Technol.* **2007**, *42*, 55−64.

(30) Lu, W.; Schmidt, H. *Adv. Powder Technol.* **2008**, *19*, 1−12.

(31) Pfaff, G. *J. Eur. Ceram. Soc.* **1993**, *12*, 159−164.

(32) Sun, X.; Shi, Y.; Zhang, P.; Zheng, C.; Zheng, X.; Zhang, F.; Zhang, Y.; Guan, N.; Zhao, D.; Stucky, G. D. *J. Am. Chem. Soc.* **2011**, *133*, 14542−14545.

(33) Xiong, Z.; Dou, H.; Pan, J.; Ma, J.; Xu, C.; Zhao, X. S. *CrystEngComm* **2010**, *12*, 3455−3457.

(34) Li, B.-h.; Tang, Y.-w.; Luo, L.-j.; Xiao, T.; Li, D.-w.; Hu, X.-y.; Yuan, M. *Appl. Surf. Sci.* **2010**, *257*, 197−202.

(35) Buscaglia, M. T.; Leoni, M.; Viviani, M.; Buscaglia, V.; Martinelli, A.; Testino, A.; Nanni, P. *J. Mater. Res.* **2003**, *18*, 560−566.

(36) Köferstein, R.; Abicht, H.-P.; Woltersdorf, J.; Pippel, E. *Thermochim. Acta* **2006**, *441*, 176−183.

(37) Rouquerol, J.; Avnir, D.; Fairbridge, C. W.; Everett, D. H.; Haynes, J. H.; Pernicone, N.; Ramsay, J. D. F.; Sing, K. S. W.; Unger, K. K. *Pure Appl. Chem.* **1994**, *66*, 1739−1758.

(38) Rouquerol, F.; Rouquerol, J.; Sing, K. *Adsorption by Powders and Porous Solids*; Academic Press: London, U.K., 1999.

(39) Stock, S.; Cullity, B. *Elements of X-ray Diffraction*; Prentice Hall: Upper Saddle River, NJ, 2001.

(40) Shi, Q.; Snow, C. L.; Boerio-Goates, J.; Woodfield, B. F. *J. Chem. Thermodyn.* **2010**, *42*, 1107−1115.

(41) Shi, Q.; Boerio-Goates, J.; Woodfield, B. F. *J. Chem. Thermodyn.* **2011**, *43*, 1263−1269.

(42) Epifani, M.; Alvisi, M.; Mirenghi, L.; Leo, G.; Siciliano, P.; Vasanelli, L. *J. Am. Ceram. Soc.* **2001**, *84*, 48−54.

(43) Sladkevich, S.; Gutkin, V.; Lev, O.; Legurova, E.; Khabibulin, D.; Fedotov, M.; Uvarov, V.; Tripol'skaya, T.; Prikhodchenko, P. *J. Sol−Gel Sci. Technol.* **2009**, *50*, 229−240.

(44) Udawatte, C. P.; Kakihana, M.; Yoshimura, M. *Solid State Ionics* **1998**, *108*, 23−30.

(45) de Kergommeaux, A.; Faure-Vincent, J.; Pron, A.; de Bettignies, R.; Malaman, B.; Reiss, P. *J. Am. Chem. Soc.* **2012**, *134*, 11659−11666.

(46) Collins, G. S.; Kachnowski, T.; Benczer-Koller, N.; Pasternak, M. *Phys. Rev. B: Condens. Matter* **1979**, *19*, 1369−1373.

(47) J. Clark, I.; Takeuchi, T.; Ohtori, N.; C. Sinclair, D. *J. Mater. Chem.* **1999**, *9*, 83−91.

(48) Guo, F.-a.; Li, G.; Yang, N.; Wang, W.; Zhang, W. *Appl. Phys. A: Mater. Sci. Process.* **2012**, *107*, 813−817.

(49) Bajnoczi, E. G.; Czegledi, E.; Kuzmann, E.; Homonnay, Z.; Balint, S.; Dombi, G.; Forgo, P.; Berkesi, O.; Palinko, I.; Peintler, G.; Sipos, P.; Persson, I. *Dalton Trans.* **2014**, *43*, 17971−17979.

(50) Gotić, M.; Musić, S.; Ivanda, M.; Šoufek, M.; Popović, S. *J. Mol. Struct.* **2005**, *744−747*, 535−540.

(51) Yu, J.; Kudo, A. *Adv. Funct. Mater.* **2006**, *16*, 2163−2169.

(52) Balamurugan, K.; Harish Kumar, N.; Ramachandran, B.; Ramachandra Rao, M. S.; Arout Chelvane, J.; Santhosh, P. N. *Solid State Commun.* **2009**, *149*, 884−887.

(53) Shi, Q.; Boerio-Goates, J.; Woodfield, K.; Rytting, M.; Pulsipher, K.; Spencer, E. C.; Ross, N. L.; Navrotsky, A.; Woodfield, B. F. *J. Phys. Chem. C* **2012**, *116*, 3910−3917.

(54) Boerio-Goates, J.; Li, G.; Li, L.; Walker, T. F.; Parry, T.; Woodfield, B. F. *Nano Lett.* **2006**, *6*, 750−754.

(55) Shi, Q.; Park, T.-J.; Schliesser, J.; Navrotsky, A.; Woodfield, B. F. *J. Chem. Thermodyn.* **2014**, *72*, 77−84.

(56) Snow, C. L.; Shi, Q.; Boerio-Goates, J.; Woodfield, B. F. *J. Chem. Thermodyn.* **2010**, *42*, 1136−1141.

(57) Woodfield, B. F.; Wilson, M. L.; Byers, J. M. *Phys. Rev. Lett.* **1997**, *78*, 3201−3204.

(58) Majzlan, J.; Navrotsky, A.; Woodfield, B. F.; Lang, B. E.; Boerio-Goates, J.; Fisher, R. A. *J. Low Temp. Phys.* **2003**, *130*, 69−76.

(59) Phillips, N. E. *CRC Crit. Rev. Solid State Sci.* **1971**, *2*, 467−553.